INTELLIGENT SOLAR MAPPING TOOL

An Undergraduate Research Scholars Thesis

by

ADEKUNLE ADEPOJU

Submitted to Honors and Undergraduate Research
Texas A&M University
in partial fulfillment of the requirements for the designation as an

UNDERGRADUATE RESEARCH SCHOLAR

Approved by
Research Advisor: Dr. C.K Madsen

May 2015

Major: Electrical Engineering

TABLE OF CONTENTS

ABSTRACT

Intelligent Solar Mapping Tool. (May 2015)

Adekunle Adepoju
Department of Electrical and Computer Engineering
Texas A&M University

Research Advisor: Dr. C.K Madsen
Department of Electrical and Computer Engineering

The goal of this thesis is to develop an overall cost effective methodology for local tracking and measuring solar patterns and intensities, for example in use in solar concentration and measurement. The idea is to create a system that is modular, cheap, and easy use. Solar trackers serve many functions in that they allow for the scientist to get an idea of irradiance patterns for studies and other more specific uses such as determining the most efficient orientation of solar capture devices. The thesis focused mainly on raw data collection and visualization. So the main challenges were to obtain the quickest and most accurate solar map. This meant deciding between having multiple sensors (photodiodes) versus fewer mobile sensors on movable axes. Using an open-source microcontroller, motors, and photodiodes, different configurations were attempted. It was discovered that better control could be obtained from having fewer sensors mounted on a two-axis system, and then varying the orientation of the sensors based on the region of space to be observed. The final system works scans a hemispherical surface by sweeping the detector head along two polar axes and storing the irradiance (as voltages) at each point. Furthermore, it works a shadowband radiometer with a spectral response range of 400nm to 1100nm. The sensor uses 10 degree half-angle photodiodes and a custom pyranometer connected to a variable gain 16-bit ADC. This allows for versatility for use during different

conditions. The results showed the system built was capable of performing a full run at a dynamic range of about 54dB with a sample density varying from 13 to 28804 data points per run, elapsing 0.0001 seconds to 17 seconds depending on the mode of operation. To test the system, spatial dependence test (for the pyranometer component) and total diffuse-direct ratio tests were carried out. The future plan is to extend the concept to solve more advanced problems such as determining diffuse versus direct components of solar radiation.

CHAPTER I

INTRODUCTION

It is highly important that a solar measurement system be efficient and capable of detecting and capturing aberrant patterns of incoming light [1] [2]. More specifically, in building a solar tracking system, it is important that one accounts for the diffuse component of light due to atmospheric conditions [2]. As seen in *Figure 1*, diffuse light is inevitable and on cloudy days, the diffuse component of incoming solar radiation may account for over seventy percent of incoming light [3].

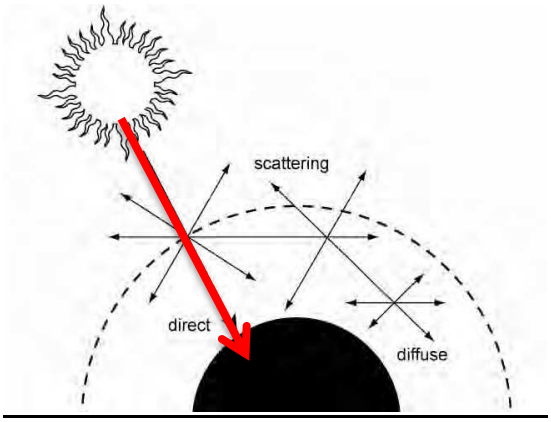

Figure 1. Naturally the direct component is more evident.

This paper targets the shadowband radiometer and attempts to improve upon it and also add more features. The shadowband radiometer is a simple method of approximating the diffuse and direct components of solar radiation. This is useful in fields such as solar concentration and tracking. So as to allow for flexibility, most of the burden of control is placed in software rather

than in hardware, and although this has some speed trade-offs, it provides immense amount of variability.

Objective

Create a device to diffuse vs direct irradiation under diverse conditions

Besides simply identifying the amount of direct and diffuse components, the nature, spatial distribution, temporal distribution, rate of change and many other factors of the solar patterns are of interest. This need for more accurate data maps is the motivation behind the project.

Methodology

Using and augmenting existing methods of measuring diffuse and direct irradiation, a tool is constructed to accomplish the objective stated above.

To achieve the desired goals, the following procedure will be taken:

Research

I. Review past and current attempts at similar goals.
II. Research methods of power optimization.
III. Explore types and properties of various apertures, motors, sensors.
IV. Obtain information on how to account for solar deviations.
V. Obtain geographical and atmospheric information specific to current area of testing (College Station, Texas).
VI. Learn appropriate methods of programming electromechanical systems.

Modelling

I. Model optical systems to visualize methods maximizing solar characterization.

II. Mathematically describe the desired system and its outputs.

III. Characterize atmospheric patterns in relation to the desired system's scope.

IV. Design a control system involving geographic and atmospheric factors.

Building and Testing

I. Build device based on most feasible model.

II. Test device under various atmospheric conditions.

CHAPTER II

METHODS

Introduction

This method uses a custom pyrometer in conjunction with a series of narrow-angle photodetectors constantly covering a semi-circular arch above the pyranometer. This system was considered to improve some simple shadowband radiometer by adding the ability to easily tell the direction of maximum incidence as well as the incident intensity distribution. Furthermore, this method allows one to exploit the benefits of a shadowband radiometer (due to the servo), with the flexibility of viewing a full hemispherical map. See *Figure 2* below.

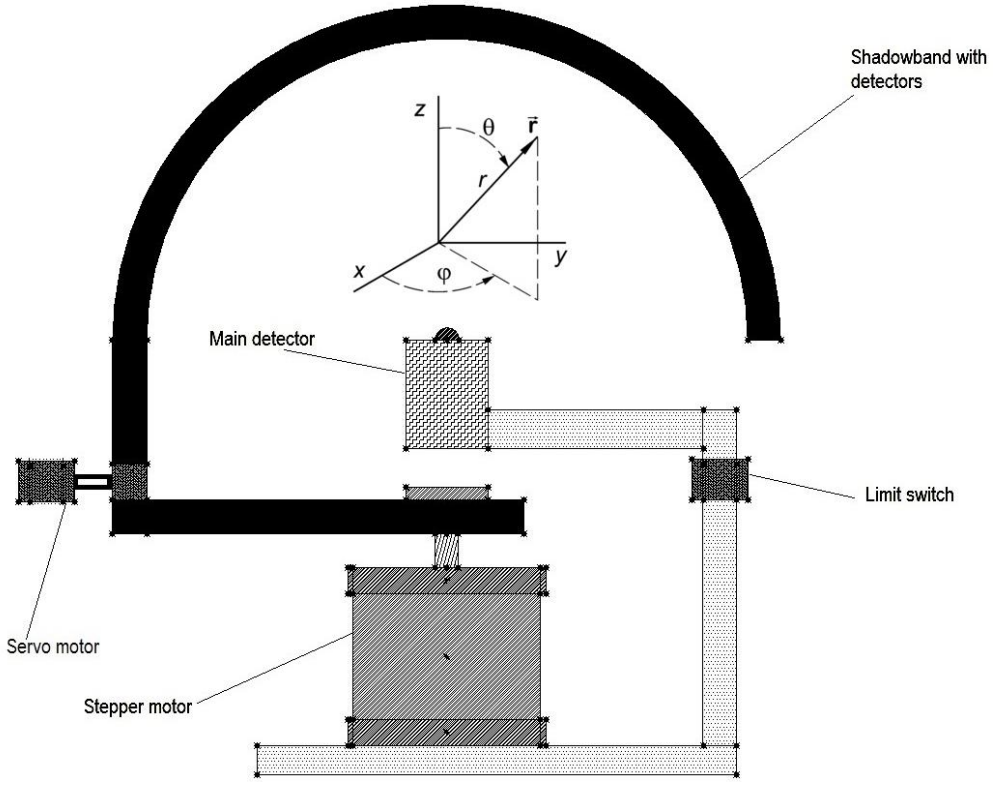

Figure 2. Diagram of device.

The system consists of a main detector (pyranometer) and a band (directly above the main detector) with nine narrow-angle photodiodes (10 degrees). This band is coupled to the stepper motor shaft for the θ-axis and is allowed 90 degrees is two directions, and a servo for the φ-axis. This system relies on the shadowband method [8] of measuring diffuse vs direct solar radiation.

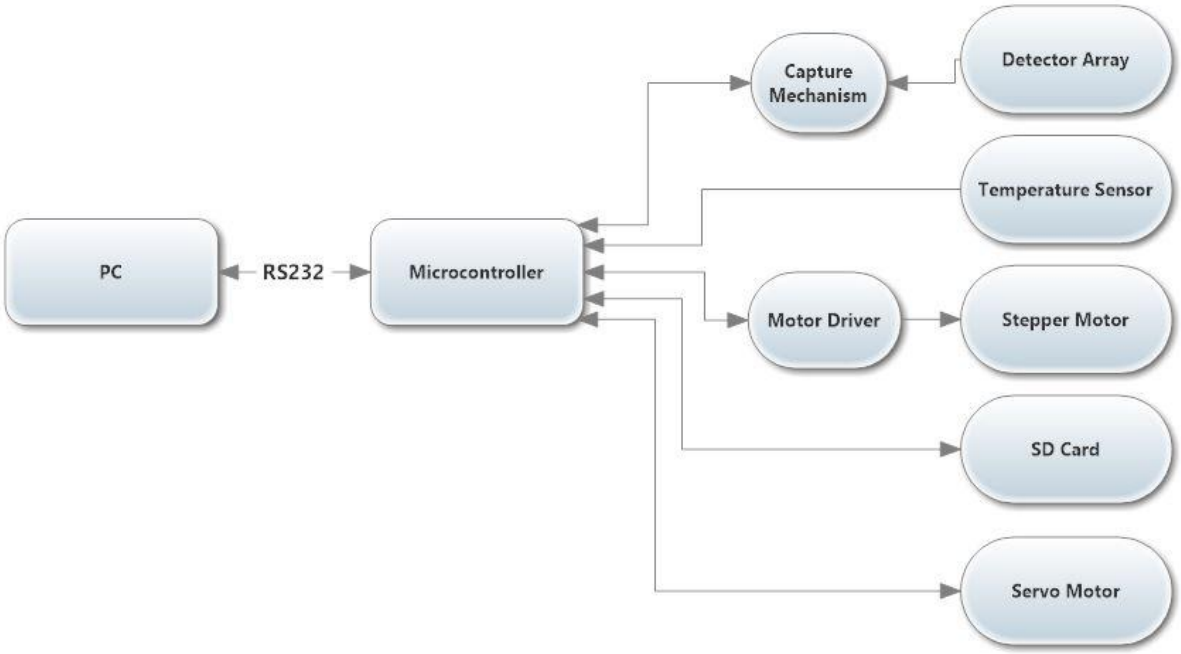

Figure 3. Flowchart of information in the system.

This system uses a microcontroller to control the stepper motor at specified intervals, while reading (and gain-adjusting) the ten detector array though 16 bit ADCs. Furthermore, a temperature sensor is included for correcting the thermal effects on photodiode behavior. In future, a heating element will be added to fix the temperature. As the microcontroller samples data, it stores the raw data in an SD card and dumps it to a PC on request through a USB-based serial interface. The PC does all of the analyses and calculations after data is accumulated. Although this means data cannot be visualized in real-time, it allows for a compact system since

a high computing machine doesn't have to be deployed at all times. The PC uses a custom made C# interface for communicating and visualizing the data. *Figure 3* shows the process layout.

Important Components

1. Photodetectors

The main detector used has a fairly broad spectral range of 400nm to 1100nm and a ±10 degree half-angle. This photodiode is coupled with Teflon as a diffuser. This allows for a pyranometer-like behavior, hence permitting light to be captured from a flat plane, similar to that used in a shadowband radiometer [7]. The system is placed in 12mm thick medium density fiberboard (MDF) for insulation and has an external metal casing. *Figure 4* shows a cut-away of the main detector.

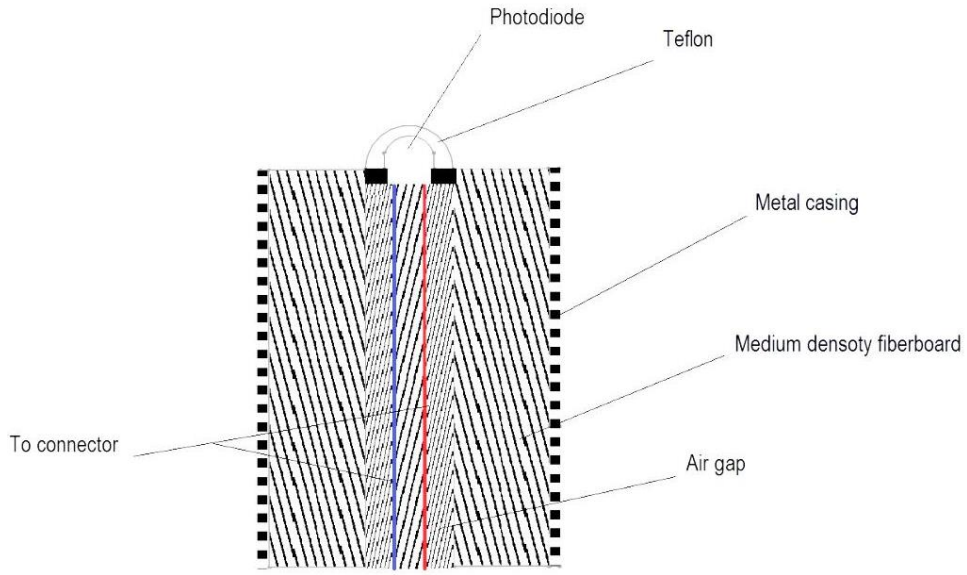

Figure 4. Detector cut-away.

The other nine secondary detectors use the same narrow-angle photodiode and are all connected to one central circuity for reading the values. The spacing is 180/8 degrees between adjacent

secondary detectors as shown in *Figure 5*. The additional photodiodes help in classifying atmospheric conditions.

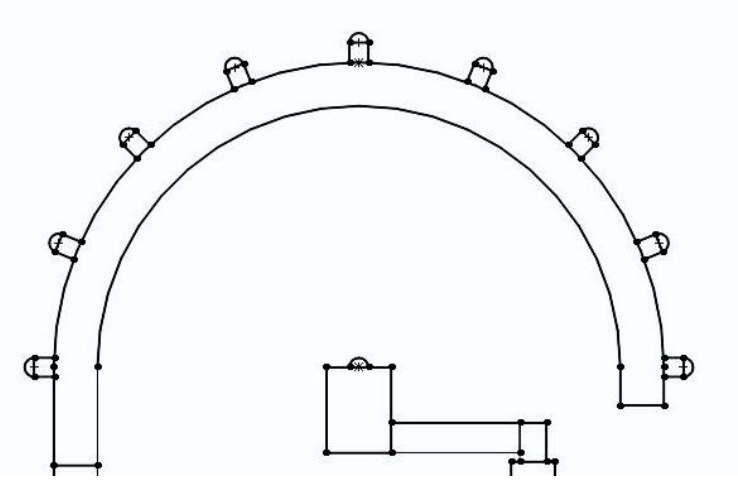

Figure 5. Arrangement of secondary detectors on arch.

2. Capture Mechanism

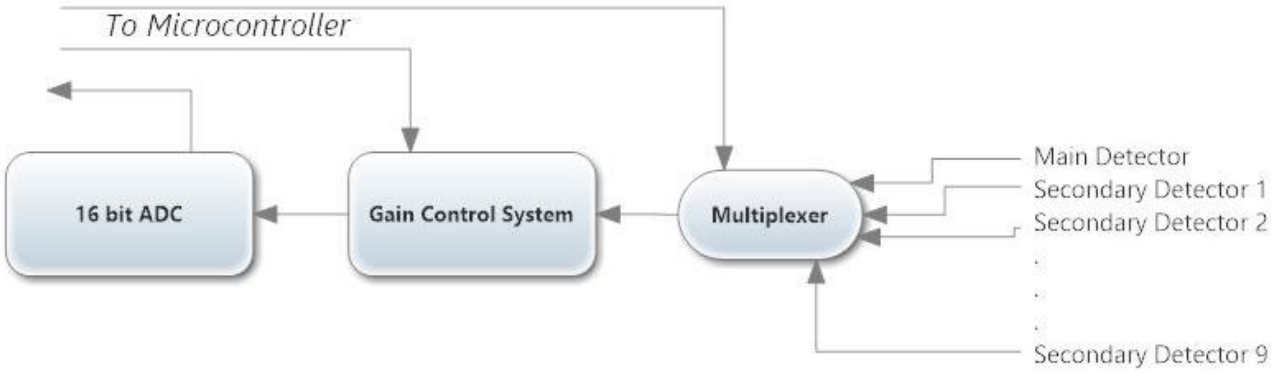

Figure 6. The flow and conditioning of captured outputs from the detector.

This consists of a digitally controlled 16 to 1 multiplexer, a gain-control system and a 16 bit ADC for reading the detector outputs. The multiplexer was chosen to have very low latency so as to increase capture speed. The ADC features gain setting from 2/3 to 16 times in input signal and

this is useful as it can be changed though software. As shown *Figure 6*, the microcontroller determines dynamically what the gain or selected detector should be.

3. TB6560 Stepper Motor Driver

With support for up to 3 amps, direction control, and overshoot control, this driver is a very good fit for the system. Cooling is also never an issue, but a downside is the bulky size. It features fast (up to 100 kHz) micro-stepping settings of up to 1/32 of the default 1.8 degree step of the NEMA 17 motor. In *Figure 7* the driver is shown (switches on the right side are for current and step adjustment).

Figure 7. The stepper motor driver.

4. Shadowband

The shadowband (or arch) is a very important component of the system and its dimensions must be chosen carefully. According to Michalsky, an umbral angle Zp of 3.27 degrees is sufficient to

block the main detector. As a result, the width of the arch (as viewed from above) as a function of the arch radius L should is described in (1) below

$$w = L * \tan(3.27\ deg) \quad (1)$$

The shadowband is also intended to be lightweight so that it can be moved by the stepper motor and swung by the servo. The servo will need to tilt the arch to ±90 degrees, and ±Zk. The angle Zk is introduced for correcting over/under-estimations due to excess coverage of the main detector [7] and is chosen as 9 degrees in this project.

Calibration

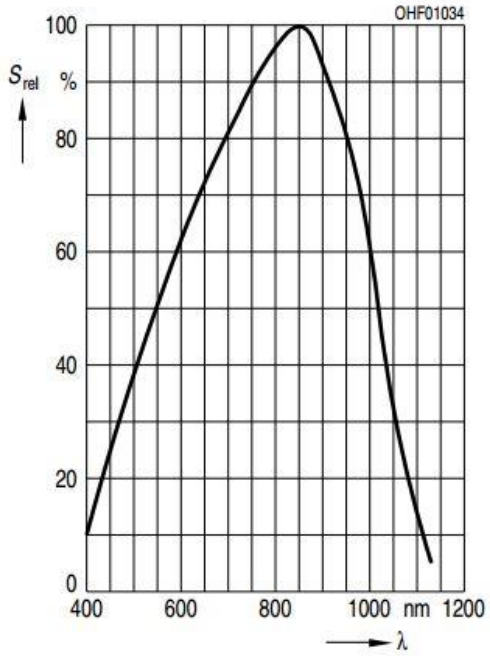

Figure 8. Sensitivity of the photodiode at different wavelengths. The peak is around 870nm.

An important step was to calibrate the components –the detectors in particular. It is important to note that although a temperature sensor was used; all tests were done at a fairly similar temperature so as to simplify the analyses. The photodiode in use had a peak sensitivity of 0.65A/W at 870nm and 25 degrees Celsius. For coherence, the wavelength used for testing was chosen to be the same for both main and secondary detectors, hence 870nm as shown in *Figure 8*. This was done for simplicity, but with better detector mechanisms, the wavelength response is to be increased to cover a broader range. The overall sensitivity seemed to remain consistent even after the Teflon was applied, so there was no need to retest.

To verify that the main detector was operating as a pyranometer, the main test conducted was to observe the deviation from the expected cosine response of a pyranometer. This test was done by using a stepper motor to move the incident light from a 5mW laser to different angles on the main detector. This test was carried out with a geared stepper motor at a resolution of 0.00009 degrees per step.

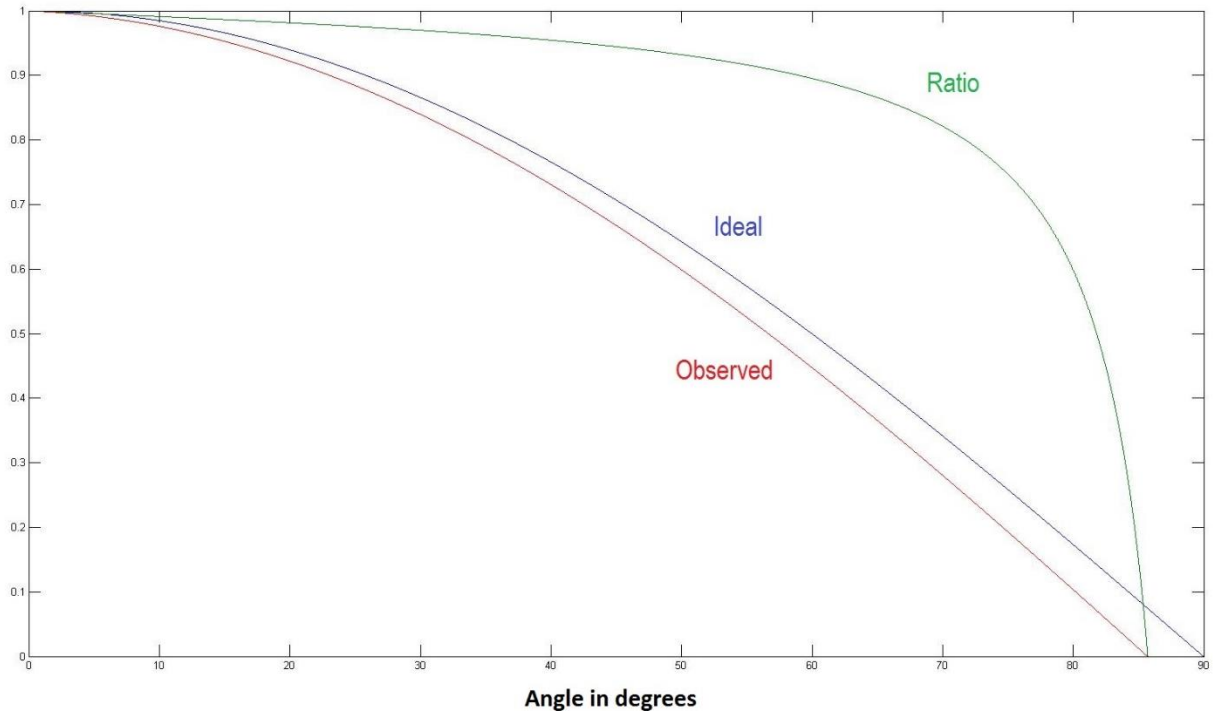

Figure 9. A curve-fitted illustration of the observed cosine response (red), contrasted with the ideal response (blue).

A proposed system for testing the dynamic range of the detectors is to sweep a calibrated laser beam and measure the response. This was attempted with multiple small lasers (due to lack of equipment), but a good beam focus was difficult to attain.

Control and Operation

The operational principle is fairly simple: the main detector captures all or some of the incident light (depending on the servo), while the secondary detectors help identify the direction and magnitude of maximum power (direct). The arch moves a maximum of 180 degree sweep at evenly spaced angular intervals (frames) while reading the detector outputs and the servo moves the arch only at the start of a series of frames. This is stored as one batch/pass. Each frame

involves multiplexing through each detector and saving the voltage read. The choice of the number of frames is varied if resolution is preferred over operation time and vice versa. The incremental angle as a function of frame count n_f and max sweep angle θ_{max} is then given as

$$\theta_s = \frac{\theta_{max}}{n_f} \quad (2)$$

θ_{max} is allowed to vary because if the sun path of the sun is known for that period of the year, there's no need to sweep across other hemispherical slices that are not of interest. In the general case where the system knows no information about the solar/weather structure, θ_{max} is 180 degrees.

Gain control is only done when switching from the main detector to a secondary detector or vice versa. This is done because the pyranometer captures more light than the secondary detectors; hence the main detector uses a lower gain setting than the secondary detectors. Timing is controlled by using a 16-bit timer in the microcontroller to precisely specify when data should be captured, and when the arch should advance. The multiplexer and gain control are varied by using digital signals (for the analog 16 to 1 mux) and I2C for the gain system. The Adafruit ADS115 has two software controlled gain settings that are changed as needed.

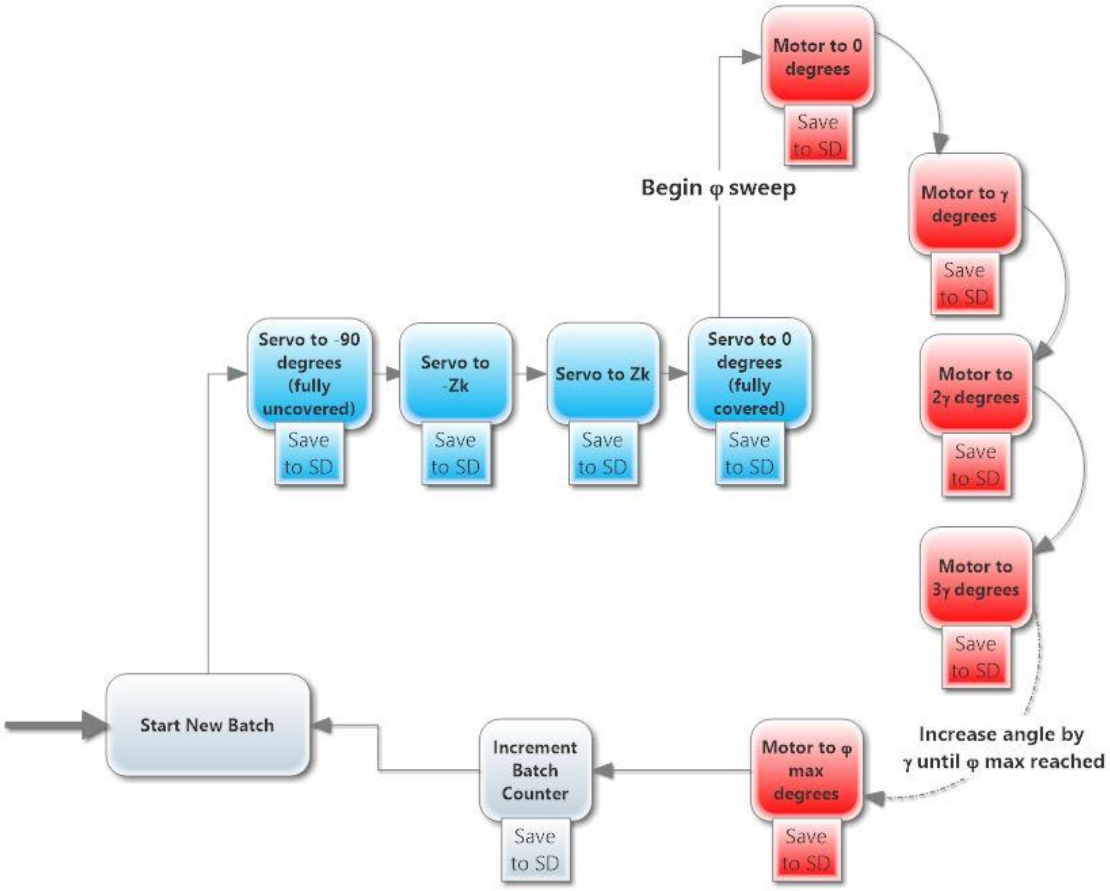

Figure 10. Operational diagram for a whole batch servo stage and frame stages. Each red portion is a new frame.

Each batch contains one 16-bit batch number, four servo readings (blue portion of image) and n_f frame readings (red portion of image), where each reading comprises ten 16-bit ADC values (one from the main detector and nine from secondary detectors). Hence one batch contains a total number of samples

$$n_s = 1 + 4 + (10 * n_f) = 5 + (10 * n_f) \quad (3)$$

while the space occupied by one batch is $n_s * 16\ bits$ or $2n_s\ bytes$.

The frequency of sampling f_s can be adjusted and even made dynamic for servo and frame readings. The hold time T_h is the time required for the system to be stationary so that all the detectors can be read. Hence one batch will run for

$$t = n_s * (\frac{1}{f_s} + T_h) \quad (4)$$

These elements of control can be varied from the PC, so as to achieve various levels of flexibility. Besides the automated control, one can specify exactly where the arch should be by sending the appropriate commands to the microcontroller. This helps when debugging and calibrating. On request, the data from the SD card is dumped to the PC at a speed of up to 2 mbps.

Analyses

The system phases can either be fully covered (θ = 0; true for all frames), partially covered ($\theta = \pm Z_k$), or uncovered ($\theta = -90\ degrees$). The uncovered phase is used for obtaining the total incident (global) irradiance Q_T, while the partially covered phases are used for obtaining data for correction of excess sky blocked in the uncovered phase [7]. The fully covered phase is for sweeping a hemisphere, determining the location of maximum incidence, and ultimately finding the diffuse component Q_D. The data obtained here can also be used to correct some of the drawbacks of the pure shadowband radiometer.

Since the global irradiance is the sum of the direct component Q_I, and the direct component, the direct component

$$Q_I = Q_T - Q_D \tag{5}$$

$Q_D$is obtained as a function of Q_{PC} the average partially covered power (average of Q at +Zk and -Zk) and $Q_C$the covered power by using the Michalsky and Wesley method. Furthermore, to improve accuracy and understand the distribution of the irradiance, values $q_{i,j}$of the secondary detectors can be analyzed (where *i* is the detector value from 0 to 8, and *j* is the frame number). Hence

$$Q_I = Q_T - Q_D(\vec{q}, Q_{PC}, Q_C) \tag{6}$$

Construction of the function $Q_D(\vec{q}, Q_{PC}, Q_C)$ requires considering the dimensions of the arch and constructing an algorithmic model of the system. A simple approximation based on Michalsky's is

$$Q_D(\vec{q}, Q_{PC}, Q_C) = Q_C + Q_T - Q_{PC} \tag{7}$$

Hence

$$Q_I = Q_{PC} - Q_C \tag{8}$$

The relative simplicity of this equation and its tendency to ignore many factors [9] was the motivation for adding the secondary detectors. The direct beam flux on a normal surface is calculated by dividing the incident intensity by the cosine of the angle where the maximum power is detected [7]. Hence

$$H = \frac{Q_I}{\cos(\angle \max(\vec{q}))} \tag{9}$$

Since nine secondary detectors are used, there's a need to interpolate for missing spots between each detector and this is done by simply average every reading nearest to that point for a total of six points averaging to one as explained below:

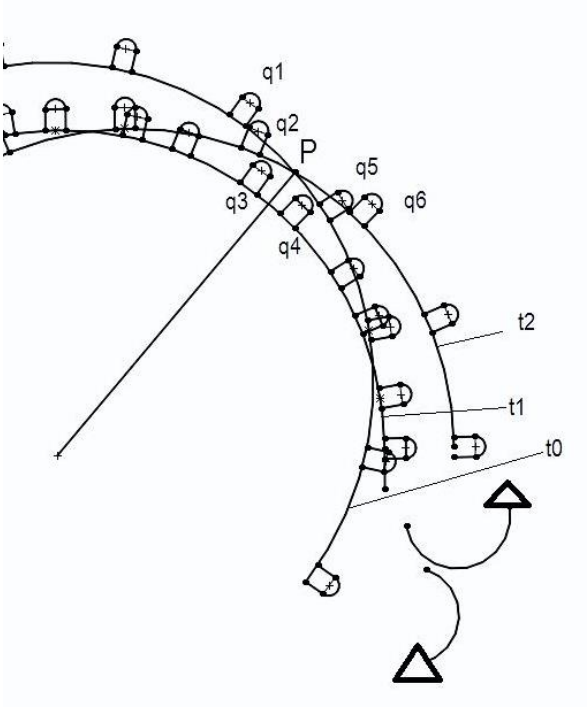

Figure 11. Time lapse diagram of arch motion. The arrows show the motion of arch t1 (t0 before, and t2 after).

Approximating the value at point P (*Figure 11*) observed at t1, is done by averaging the left and right values observed before t1 (at t0) with the values at t1 and also after t1 (at t2). Hence all six values around that point are averaged.

Hence

$$Q_P = \frac{q1+q2+q3+q4+q5+q6}{6} \quad (10)$$

This is done recursively on the PC to improve visualization detail. Although three dimensional visualization is still being created, it is possible to view the data points in 2D using a C# program. The main reason for using C# as against C++ (which is faster) was due to ease of serial port integration and graphics.

CHAPTER III

RESULTS

Based on how many frames are required, the time elapsed can vary from 100us to over 17s because of motor delays and servo speeds. For operation as a simple shadowband radiometer (hence stationary stepper motor), the time taken is simply how long it takes to sweep the servo plus 400us (100us for each capture: -90, -Zp, 0, Zp). This comes out to about 800ms. The stepper motor was set to hold the system when idle, hence drawing power. This seems inefficient but is important to prevent the arch from swinging arbitrarily. The continuous power consumption varied from 7.3 watts to 8.6 watts.

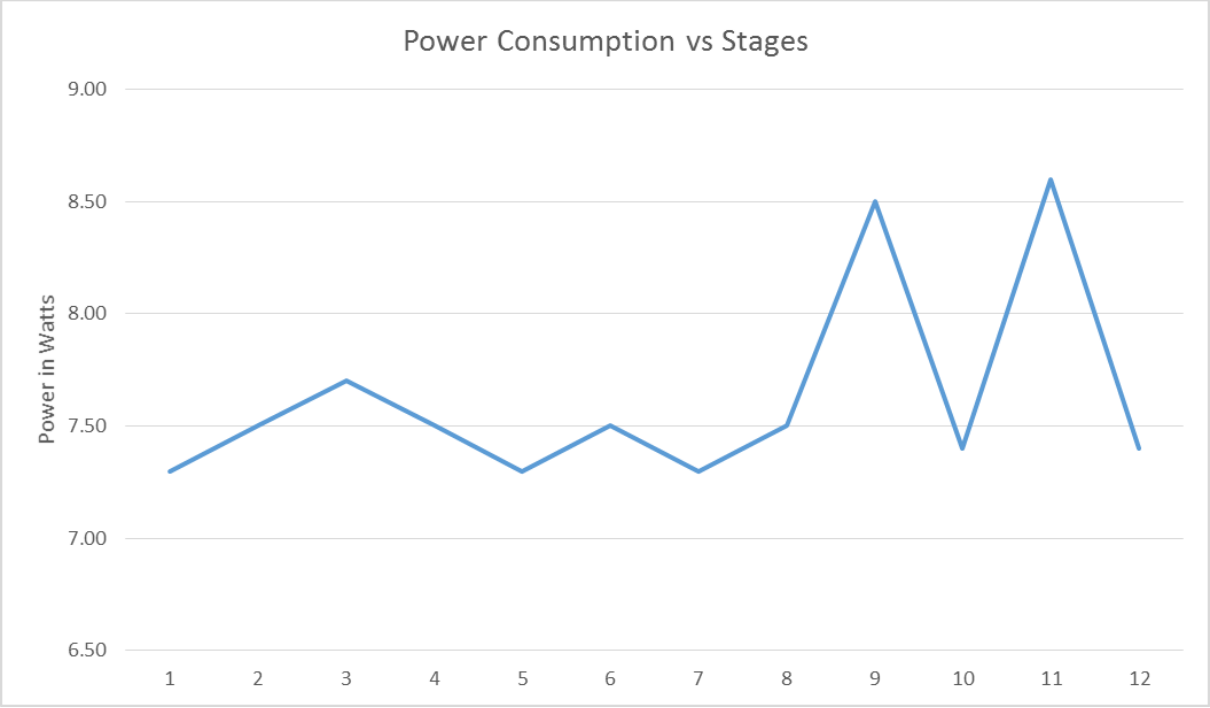

Figure 12. Power consumption in Watts at different stages.

The first 8 stages show servo motion, while the stepper motor is holding its position (hence consuming power). From stage 9, the power undulates as the stepper motor alternates between holding and moving. Reducing the weight of the materials will have an effect on the power consumption as this will in turn reduce the holding power consumption of the stepper motor. This is important so that a battery can be used to power the system.

It was difficult to verify the spectral range of the detectors due to not having a way to seep the entire 400nm to 1100nm range, but testing close to both extremes (with blue LED light and IR light) showed some level of responsivity.

A major fact that was ignored in these tests were the effects of ambient temperature. Most experiments were carried out at fairly constant temperature and were not long enough for self-heating to be a problem. But temperature compensation (either through mathematical adjustments or through ambient temperature control) is a major step to be accomplished.

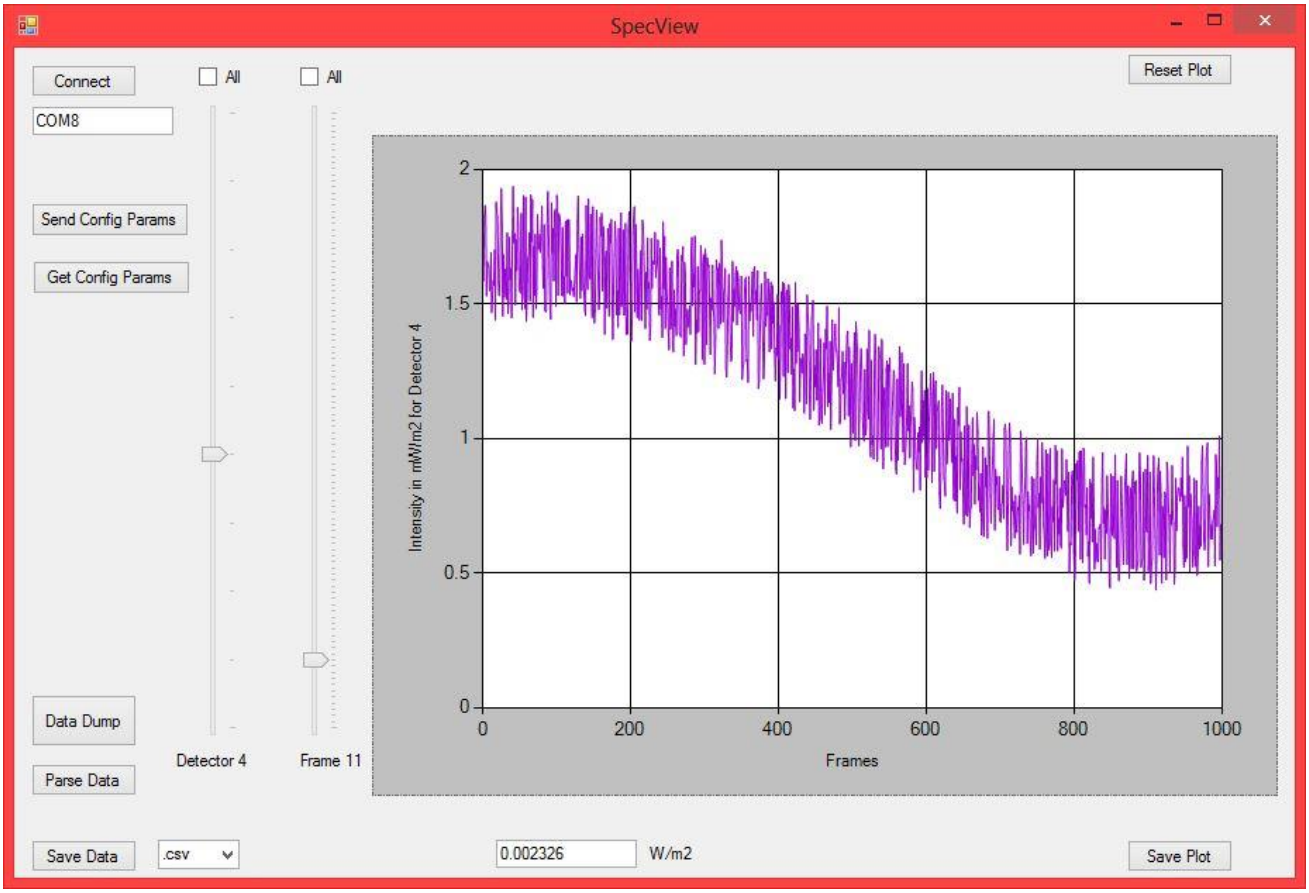

Figure 13. PC program showing the outputs at each frame for one detector.

This simple program shown in *Figure 13* allows visualization of individual data points or frames of points per detector. The system connects to a PC over USB and the program is designed to work with Microsoft Operating system Windows 7 and up. Using the sliders, one can select which detector output to view. When detector 0 (main detector) is selected, the plot switches to a mode that allows easy visibility of $Q_I, Q_D, and\ Q_T$, as shown in *Figure 14.*

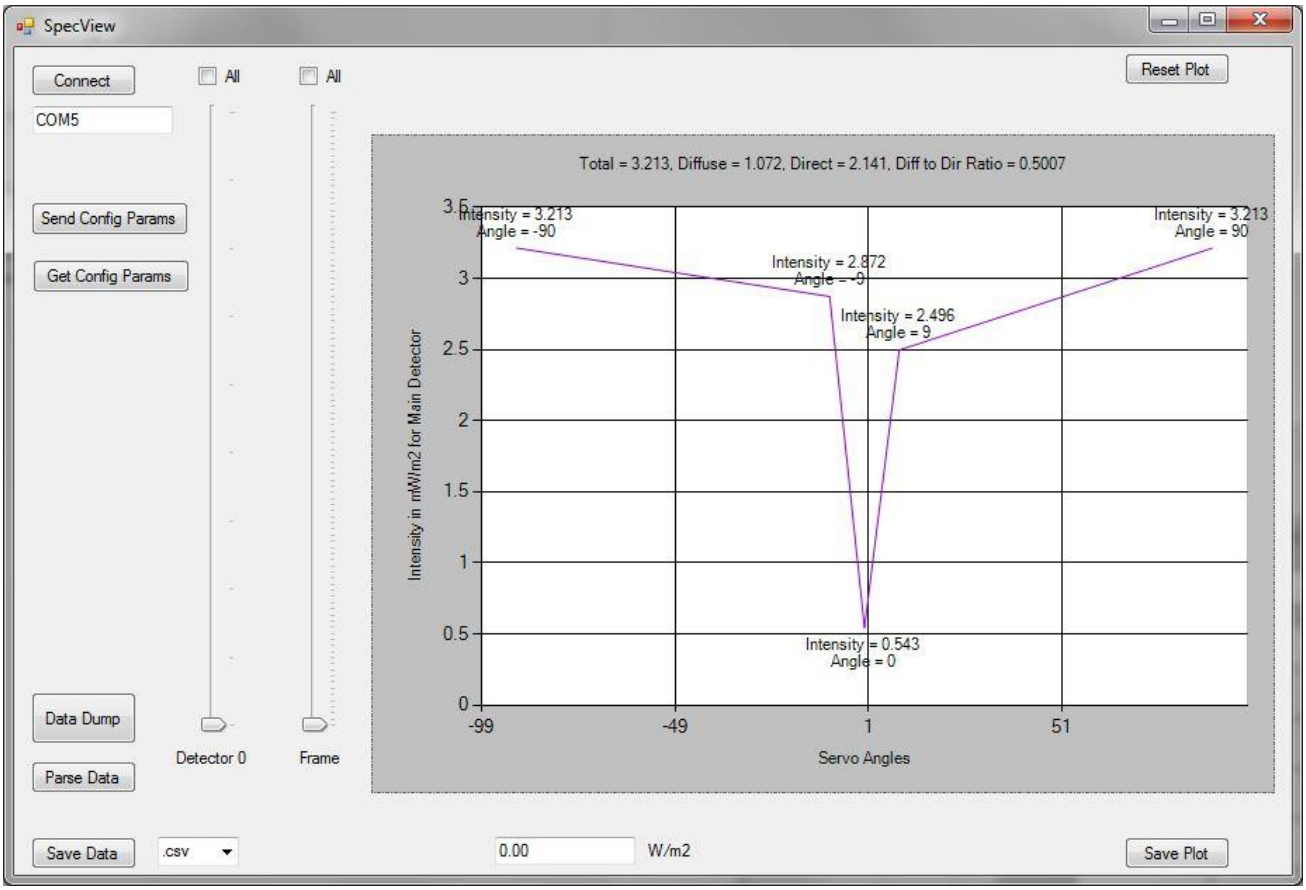

Figure 14. The shadowband mode (detector 0) displayed in the PC program. The points of interest are labelled.

In the image above, the expected shadowband characteristic plot is seen. This is a plot purely obtained from the servo phase without any correction from the secondary detectors.

CHAPTER IV

CONCLUSION

The system designed here definitely shows a lot of potential and a strong proof of concept. With improving designs, the goal is to solve problems with latencies, power efficiency, and acurracy. There's also a strong drive to improve visualization of the output data so it coveys more information. It should be noted that the system does not currently offer the accuracy of post processing and corrections that a high end system will provide. There still exists a lot of work to be done in improving capture accuracy and efficiency. A downside to the current system is that data has to be post-processed. This does not allow for real-time visualization of the data. To correct this, a more lightweight system is being developed in C++ to run on a microcontroller, or to simply transfer the data in real-time to a mini-computer. Nonetheless, some data needs to be post-processed due to the complexity that naturally arises when dealing with large volumes of data, so the usage of GPUs to aid computation is being explored. Regarding cost of implementation, the proposed system discussed here is much cheaper and more flexible since the parts are modular and an open source microcontroller framework is used. This allows for ease of access of software understanding and advancement.

REFERENCES

[1] Madsen, C. K., Schulz, A., Wu, W., Sosa A., Huang R., Mohamed, T., Atkins R., and Simcik J "A Small-scale Concentrating Solar Thermal System." CSP Systems and Optics (2014): 1-3. Spie.org. Web

[2] Wenham, S. R., A. M. Green, and M. R. Watt. "THE CHARACTERISTICS OF SUNLIGHT." Applied Photovoltaics. London: Earthscan, 2007. 8-10. Print

[3] Piot, Julien, Urban G. Schnell, and Philippe J. Nussbaum. Optical Detection System, Device, and Method Utilizing Optical Matching. Logitech Europe S.A, assignee. Patent US6927758 B1. 29 June 2001. Print.

[4] Wenham, S. R., Green A. M., and Watt, M. R., *Atmospheric scattering leading to diffuse radiation.* Applied Photovoltaics. London: Earthscan, 2007. 9. Print.

[5] Piszczor, M.F.; Brinker, D.J.; Flood, D.J.; Avery, J.E.; Fraas, L.M.; Fairbanks, E. S.; Yerkes, J.W.; O'Neill, M.J., "A high-performance photovoltaic concentrator array: The mini-dome Fresnel lens concentrator with 30% efficient GaAs/GaSb tandem cells," *Photovoltaic Specialists Conference, 1991., Conference Record of the Twenty Second IEEE* , vol., no., pp.1485,1490 vol.2, 7-11 Oct 1991

[6] Piszczor, M.F.; O'Neill, M.J.; Fraas, L.M., "Development of a line-focus refractive concentrator array for space applications," *Photovoltaic Energy Conversion, 1994., Conference Record of the Twenty Fourth. IEEE Photovoltaic Specialists Conference - 1994, 1994 IEEE First World Conference on* , vol.2, no., pp.2022,2025 vol.2, 5-9 Dec 1994

[7] Michalsky, J.J; Harisson, L.; Brandt,Jerry, "Development of a line-focus refractive concentrator array for space applications Automated multifilter rotating shadow-band radiometer: an instrument for optical depth and radiation measurements," *Applied Optics*" Vol.33 No 22 pp. 5118-5125, 1 August 1994

[8] Patil A.; Haria K.;Pashte P; "Phtotodiode Based Pyranometer", "*International Journal of Advances in Science Engineering and Technology*", Vol 1, Issue 1, pp.29-33 July 2013.

[9] Wesley M.L; “Simplified Techniques to Study Components of Solar Radiation Under Haze and Clouds”, “*American Meteorological Society*”, pp. 373-384, July 1990.

APPENDIX A

DATA STORAGE AND TRANSPORT

The table below shows a sample batch of data. N stands for negative, P stands for positive. Each detector value, starting from the main detector, is encoded in D0 to D9.

The first frame (Frame 0) is the frame at which servo motion is carried out (shadowband mode). After the first frame, there is no need to send servo stage information as this is recorded on once.

Each field is 2 bytes wide and the end of a batch is terminated with an empty line.

Frame Count =0	D0	D1	D2	D3	D4	D5	D6	D7	D8	D9	N90	NZp	PZp	Origin
Frame Count >0	D0	D1	D2	D3	D4	D5	D6	D7	D8	D9				

The PC checks if a 0 frame is detected to determine the start of a sequence. When parsing, it should be noted that the gains on each of the detector outputs can vary, hence they should not be equally weighted.

Data dump is done by selecting the clicking the “Data Dump” button in the program which sends a command to the microcontroller to transfer all of the SD card contents. Although the speed used was 2 mbps, there can be interruptions when transferring such large amounts of data. As a result, the data is sent twice, and compared by the PC for correctness before the PC instructs the microcontroller to erase the SF card.

APPENDIX B

PARTS LIST

Part	**Model**	**Notes**
Photodiode		
16 Bit ADC	Adafruit ADS1115	Based on the TI ADS1115 ADC
Stepper Motor	NEMA 17 stepper motor	Ensure torque is sufficient
Stepper Motor Driver	Toshiba tb6560ahq dev board	
Servo motor	Power HD High-Torque Servo 1501MG	Ensure torque is sufficient
Beam and base	½ inch MDF	3D printed parts are probably better
Photodiodes	Osram SFH213	
Microcontroller	Arduino Mega	
SD Card Module	Arduino 120801 Micro SD Card Module	